machines

MDPI

Article

Pre-Compensation Strategy for Tracking Error and Contour Error by Using Friction and Cross-Coupled Control

Minghao Liu [1], Yongmin Zhu [1], Hongliang Xu [1], Weirui Liu [1,*], Hui Yang [2,3,*] and Xingjun Gao [1]

[1] School of Mechanical Engineering, Liaoning Petrochemical University, Fushun 113000, China; 15841330518@163.com (M.L.); 18309468637@163.com (Y.Z.); 13130324609@139.com (H.X.); gaoxingjun@lnpu.edu.cn (X.G.)
[2] School of Mechatronic Engineering, Guangdong Polytechnic Normal University, Guangzhou 510665, China
[3] School of Mechanical Engineering and Automation, Beihang University, Beijing 266104, China
* Correspondence: wr_liu@lnpu.edu.cn (W.L.); yanghuibuaa1987@buaa.edu.cn (H.Y.)

Abstract: This paper focuses on improving the tracking accuracy for servo systems and increasing the contouring performance of precision machining. The dynamic friction during precision machining is analyzed using the LuGre model. The dynamic and static parameters in the friction model are efficiently and accurately identified using the improved Drosophila swarm algorithm based on cross-mutation. The friction tracking error can be deduced from the friction state space and an expression is derived. To compensate for the tracking error caused by friction, a feedforward compensation control is designed to avoid signal lag in traditional friction controllers. Furthermore, the factors of multi-axis parameter mismatching that impact the machining profile accuracy are analyzed for multi-axis control. An adaptive cross-coupled control-based pre-compensation strategy of contour error is designed to reduce both the tracking error and the contour error. The effectiveness of the proposed method is validated through several experiments, which demonstrate a remarkable improvement in tracking performance and contour accuracy.

Keywords: friction force prediction; feedforward control; contour error cross-coupled control

check for updates

Citation: Liu, M.; Zhu, Y.; Xu, H.; Liu, W.; Yang, H.; Gao, X.. Pre-Compensation Strategy for Tracking Error and Contour Error by Using Friction and Cross-Coupled Control. *Machines* **2024**, *12*, 593. https://doi.org/10.3390/machines12090593

Academic Editor: Angelos P. Markopoulos

Received: 9 July 2024
Revised: 15 August 2024
Accepted: 21 August 2024
Published: 26 August 2024

Correction Statement: This article has been republished with a minor change. The change does not affect the scientific content of the article and further details are available within the backmatter of the website version of this article.

Copyright: © 2024 by the authors. Licensee MDPI, Basel, Switzerland. This article is an open access article distributed under the terms and conditions of the Creative Commons Attribution (CC BY) license (https://creativecommons.org/licenses/by/4.0/).

1. Introduction

Tracking error is an important evaluation index for measuring the single-axis motion accuracy of a precision machining platform [1,2]. It describes the difference between the actual position and the command position, which hinders the machine tool from moving to the specified position accurately and leads to contour errors in multi-axis linkage [3]. Traditionally, methods for correcting tracking errors involve detecting the absolute position of the actuator. Although this method can reduce tracking error to some extent, it fails to meet the high-precision requirements of precision machining [4]. Therefore, it is necessary to analyze the tracking error in detail and design advanced control strategies to compensate for it. In the process of precision machining, internal factors such as servo delay, friction, thrust fluctuation, and vibration, as well as external factors like assembly, wear, and temperature, can all influence tracking error [5]. This paper focuses on internal friction disturbance, analyzes its influence on tracking error, and establishes an estimation model and control strategy. Additionally, this paper thoroughly examines contour error modeling and design strategies for control.

Friction, caused by the contact of surfaces within each mechanism, hinders the linear feeding motion of a machine tool and reduces the output accuracy and motor motion stability of the machining process. This is particularly problematic for parts with high surface quality requirements since friction disturbance can disrupt the continuity and integrity of the workpiece surface, resulting in increased RA and RMS roughness values [6]. Existing research categorizes friction into two main types: static friction and dynamic friction [7,8]. Several static models have been developed, including the Coulomb force

model [9], the static friction viscous damping model [10], Stribeck model [11], and Karnopp model [12]. However, these models have limitations in fully capturing the nonlinear dynamic characteristics of pre-sliding friction, static friction, and lag friction. On the other hand, dynamic friction models such as the LuGre model [13], Leuven model [14], and Maxwell slip model [15], are widely used due to their simple structure and strong dissipation. The LuGre model decomposes the friction process into pre-sliding and sliding stages, allowing for a comprehensive description of the static and dynamic characteristics of friction. It effectively addresses the limitations of the static friction model. However, accurate identification of static and dynamic parameters is crucial in LuGre friction modeling. Liu proposed a distributed decoupling identification method to separate the friction characteristics of the pre-sliding and sliding stages, enabling separate identification and compensation for each stage [16]. Differential evolution identification algorithms are used to accurately obtain the friction model parameters, reducing computational complexity, and ensuring global optimization performance [17]. Seung Jean proposed an autoregressive model to identify the coefficient of viscous friction in the frequency domain [18]. Furthermore, various excellent algorithms such as neural networks, least square methods, genetic algorithms, and ant colony algorithms are utilized for friction parameter identification [19,20]; these algorithms have made outstanding achievements in multi parameter recognition.

With a control strategy that predicts and compensates for friction errors, and by modeling and identifying friction parameters, along with compensating for tracking errors caused by friction using predictive control strategies, it is possible to effectively enhance the processing accuracy of machine tools. To observe the state variables, Truong's double observers are utilized to predict the nonlinear state variables in the friction process. This is combined with the advanced sliding mode adaptive control to achieve the friction compensation of the linear servo system [21]. Lin proposed an adaptive robust controller that modifies the LuGre model and incorporates a nonlinear observer to estimate the friction torque [22]. Iwasaki proposed a LuGre friction disturbance observer that includes both the static and dynamic characteristics of friction to accurately simulate the actual machining. Experimental results demonstrate that this method significantly improves the motion-tracking performance of the system [23]. Rafan, using a feedforward PID compensator, takes advantage of the static friction model and generalized Maxwell model to compensate for friction in both the sliding and pre-sliding stages, resulting in a certain degree of improvement in trajectory-tracking accuracy [24].

This study focuses on modeling friction for the precision machine tools using the LuGre model. To address the dynamic parameter identification in the model, a dynamic step-size-based cross-variation fruit fly optimization algorithm was employed for efficient and accurate identification. A friction feedforward controller was designed to offset the tracking error caused by friction, avoiding delays in the traditional friction control strategy. Additionally, a tracking error expression caused by friction was derived based on the state space. To address challenges arising from variations in axis parameter inertia that hindered direct mirror compensation of contour error values, a contour error model was established. This model was used to analyze the impact of axis parameter inertia on contour error, enabling the precise compensation of machining contour errors through a cross-coupled controller [25–28]. Compared to direct symmetrical compensation, the cross-coupled control (CCC) method was more accurate and had a more significant impact on improving machining contour accuracy.

2. Modeling and Identification of Friction

The U-type linear motor is used as the driving source of the precision platform. It improves transmission efficiency and reduces friction loss by eliminating the complicated mechanical transmission structure. However, the friction between the slider, platform, and other surface contact links cannot be completely avoided. This friction, influenced by factors such as load and weight, hinders the feed motion of the machine tool. Particularly at low speeds and during reversing, position deviations increase significantly, leading

to a decrease in overall machining accuracy. Additionally, excessive friction impacts the stability of motor thrust output. Therefore, this section analyzes the friction disturbance and tracking error caused by the friction of the linear motor.

2.1. LuGre Friction Modeling

The LuGre model is widely used in friction identification due to its ability to absorb the Stribeck effect and accurately describe friction characteristics through bristle parameters [29]. The process of precision machining involves a variety of mixed nonlinear states that can cause friction disturbances. The LuGre model [30] is described as follows:

$$\begin{cases} \frac{dz}{dt} = v - \sigma_0 \frac{|v|}{g(v)} z \\ g(v) = F_c + (F_s - F_c) e^{-(\frac{v}{v_s})^2} \\ F_r = \sigma_0 z - \sigma_1 \frac{dz}{dt} + \sigma_2 v \end{cases} \tag{1}$$

where z is average deformation of bristle, v is relative feedrate, v_s is the Stribeck speed. F_r, F_c, F_s are the friction force, Coulomb force, and maximum static friction, respectively. $\sigma_0, \sigma_1, \sigma_2$ are sideburns stiffness, damping coefficient and friction coefficient, respectively. $g(v)$ is the Stribeck function.

In the movement of a precision linear mechanism, the sliding friction is changed with different feed rates, resulting in an inconsistent surface roughness that increases the calculation difficulty of friction. The dynamic parameters $\sigma_0\sigma_1$ and static parameters v_s, F_c, F_s, σ_2 are used to exhaustively describe the friction force in this complex movement [31]. However, due to the bilateral symmetrical structure of the U-type linear motor, this paper does not consider the influence of the normal force on the friction force. Moreover, the normal thrust fluctuation between the primary and secondary can be offset, making it negligible.

$$\widetilde{z} = \frac{g(v)}{\sigma_0} \mathrm{sgn}(v) \tag{2}$$

substituting (2) into the LuGre model:

$$F_r = \left[F_c + (F_s - F_c) e^{-(\frac{v}{v_s})^2} \right] \mathrm{sgn}(v) + \sigma_2 v \tag{3}$$

Equation (3) contains the state variable $\widetilde{z}$, which can describe the friction process more comprehensively. The accuracy of parameters directly affects the accuracy of friction modeling. Therefore, the identification parameter matrix $W = ([\sigma_0, \sigma_1, v_s, F_s], t)$ is established, W_0 is the experimental parameter matrix, and the variance of deviation between the actual path and the reference path is regarded as the evaluation function:

$$e_W = \int_t \left(W_0(t) - W[\sigma_0, \sigma_1, v_s, F_s] \right)^2 dt \tag{4}$$

2.2. Multi-Parameter Identification of Friction Model

The parameters of the LuGre model can be accurately identified by addressing the limitations of conventional iterative algorithms [32], as shown in Equation (4). In order to improve the accuracy of multi-parameters synchronous identification, a new fly optimization algorithm (FOA) is proposed. The FOA enables group optimization, making it suitable for identifying the parameters of the LuGre model. By employing dynamic steps and adaptive cross mutation, the FOA effectively addresses the issue of the traditional Drosophila algorithm falling into local extremum, thereby improving the accuracy of parameter identification. The FOA mimics the predatory process of drosophila, utilizing its olfactory superiority to quickly distinguish complex odors in the air. The FOA stands out from other optimization algorithms due to its simplicity in structure, ease of programming,

faster convergence, and fewer parameters. The foraging process of the FOA is depicted in Figure 1.

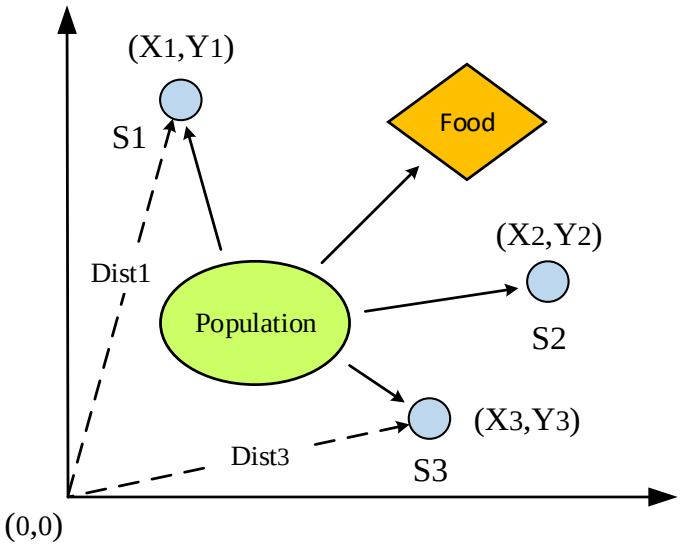


Figure 1. Iterative foraging process of fruit flies.

The adaptive crossover factor is introduced to regulate the crossover of the population to search for the global optimal value of the population. This effectively improves the adaptability of the Drosophila individual to environmental changes. The main steps involve randomly pairing the Drosophila population and selecting any pair as the parent. After crossover and mutation, the same number of offspring is generated as the parent. The cross-mutation process enhances the population diversity and the ability to jump out of local extremum.

The fitness of the N-th population of drosophila can be expressed as $f_i(i = 1, 2 \ldots N)$. The crossover probability is q and is shown as follows:

$$q = \begin{cases} q_1 - \dfrac{q_2 - q_1}{1 + e^{-2A_{con}\frac{Smell_{mid} - Smell_{avg}}{Smell_{\max} - Smell_{avg}}}}, & Smell_{mid} \geq Smell_{avg} \\ q_2, & Smell_{mid} < Smell_{avg} \end{cases} \tag{5}$$

$$\begin{cases} X_i^*(k) = qX_i(k) + (1-q)X_i(k+1) \\ X_i^*(k+1) = qX_i(k+1) + (1-q)X_i(k) \end{cases} \tag{6}$$

$$X_i(k) = X_0\left(1 + \frac{\tan(rand(0,1) - 0.5)\pi}{2}\right) \quad k = 1, 2, \ldots N \tag{7}$$

q_1, q_2 are the range of crossover probability, $Smell_{mid}$ represents the larger fitness value of two cross particles, $Smell_{max}$ is the maximum fitness in population, and $Smell_{avg}$ is the average value in population.

To maintain a certain crossover probability and obtain more excellent genetic genes, the function of constant A_{con} is used to slow down the variation trend of crossover probability q when the fitness value is high. This ensures the number of excellent offspring and improves the heritability of the dominant genes (5)~(7). Therefore, the drosophila population, which is close to the highest quality part of the whole world, can benefit from maintaining a certain crossover probability and acquiring more excellent genetic genes. As shown in Figure 2, the parameter identification process of LuGre modeling using the improved drosophila algorithm is as follows:

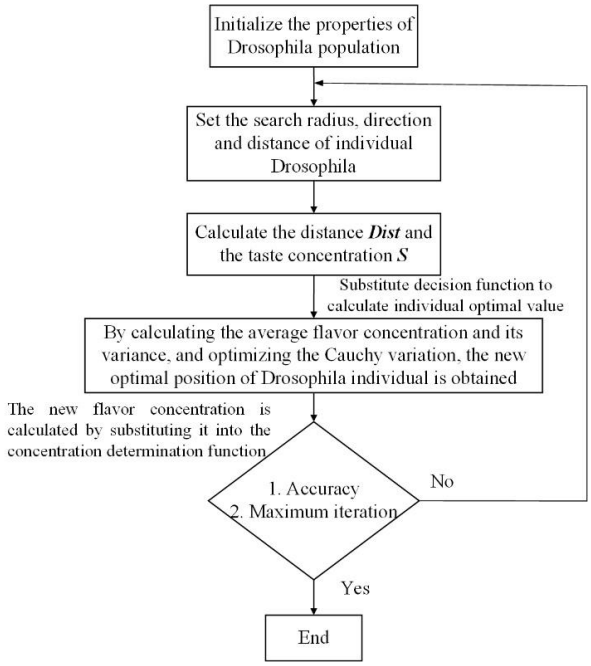


Figure 2. Flowchart of iterative evolution process.

(1) The calculation of the determination value of concentration S requires the initial population parameters, such as population size, the number of iterations (tmax), initial positions (X_pos and Y_ pos), fitness threshold (δ), search radius (R_{value}), mutation probability (q), and search direction.

To enhance both global search efficiency and local search accuracy, the proposed approach incorporates the strategy of dynamically reducing step length. Initially, a larger step length is employed to facilitate a wide range search of the entire population, enabling quick identification of the target area. As the target area is approached, the search step length and speed are gradually decreased to encourage the drosophila particles to explore the vicinity of the optimal solution in depth. Simultaneously, the issue of the population being prone to becoming trapped in local minima is addressed through the utilization of an exponential distribution function. The improved formula is as follows:

$$\begin{cases} X_i = X_{_pos} + L_s \cdot R_{Value} \\ Y_i = Y_{_pos} + L_s \cdot R_{Value} \end{cases} \tag{8}$$

$$L_s = \frac{L_{\max}}{Smellbest_{i-1}} \cdot R_i \cdot a^c \tag{9}$$

$$c = \frac{t_i + t_{\max}}{t_{\max}} - \cos\frac{t_i}{t_{\max}} \tag{10}$$

$$R_i(x) = 1 - e^{-\alpha x} \tag{11}$$

where $Smellbest_{i-1}$ is the last generation optimal flavor concentration value, L_{max} is the maximum step length, α = 0.01 is the exponential factor, t_i represents the current iterations, and R_i is the exponential distribution function that the power exponent is 0.5.

(2) The paragraph calculates the average taste concentration ($Smell_{avg}$), and the variance in taste concentration (σ^2). A smaller variance indicates a higher concentration and lower diversity within the population.

When the current fitness value Smellbest does not reach the target requirement and $\sigma^2 \leq \delta$, it can be inferred that the current population is trapped in a local extremum. In this case, if the random number (0~1) is less than the mutation probability q, the optimal positions undergo Cauchy mutation for optimization. Subsequently, the new optimal

positions of the drosophila individuals are obtained through secondary optimization of the mutated particles.

(3) The distance between the new position, the origin and the determination value of concentration is re-estimated,

$$Dist'_j = \sqrt{X^2_{posbj} + Y^2_{posbj}} \tag{12}$$

$$S'_j = \frac{1}{Dist'_j} \tag{13}$$

Substituting S'_j into taste concentration function and calculating the new taste concentration,

$$Smell_j = function\left(S'_j\right) \tag{14}$$

if $Smell'_j < Smellbest$, then $Smellbest = Smell'_j$, $X_{pos} = X_{posbj}$, $Y_{pos} = Y_{posbj}$. The flowchart shown in Figure 2 represents the iterative process described above, which is repeated until either the maximum number of iterations is reached or the desired level of accuracy is achieved. This process incorporates the adaptive crossover of drosophila, which helps to make the distribution of individuals more realistic during the optimization process. Additionally, the inclusion of a threshold and the implementation of Cauchy mutation serve to enhance the overall diversity of the population, addressing the issue of particles becoming prematurely trapped in local optima.

The advantages of the improved drosophila algorithm were demonstrated through the iterative evolution curve shown in Figure 3 and the parameter identification results (average value) displayed in Table 1 and the standard deviation shown as Table 2. Figure 3 revealed that the improved drosophila algorithm exhibited faster convergence speed and higher efficiency. To further highlight these advantages, three traditional algorithms were compared. The identification algorithm proposed in this paper achieved higher accuracy, the estimated errors of dynamic parameters $\boldsymbol{F_s}$, $\boldsymbol{v_s}$, $\boldsymbol{\sigma_0}$, and $\boldsymbol{\sigma_1}$ were 0.4%, 0.4%, 1.6% and 0.07%, respectively. The maximum was only 1.6% and other algorithms were all larger than the proposed method as shown in Table 1, and the standard deviations in Table 2 were all smaller than the other algorithms. This method was more suitable for the multi-parameter synchronous identification of the LuGre model compared to traditional iterative algorithms. In the unloaded state of the machine tool, a uniform reciprocating motion was established. The signal acquisition system measured the feeding current values and the feed rate of the linear motor during both forward and reverse motions. These data allowed for the derivation of the friction torque and the Stribeck scatter plot shown in Figure 4. Depending on the consistency of the methodology, this study concentrated exclusively on the friction occurring during forward feeding. The detail parameters of machine tool were $\boldsymbol{F_s}$ = 20.53 N, vs. =61.05 mm/min, $\boldsymbol{\sigma_0}$ = 364.18 N/mm, $\boldsymbol{\sigma_1}$ = 181.20 N/(mm/s).

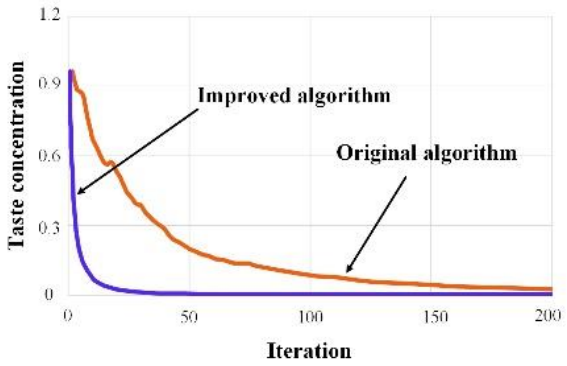


Figure 3. Comparison of iterative evolution curves.

Table 1. Identification results of friction parameters.

	Design Values	Least Square Algorithm	Genetic Algorithm	Ant Colony Algorithm	Proposed Algorithm
F_s (N)	30.00	30.51	30.63	30.21	30.12
v_s (rad/s)	0.500	0.479	0.485	0.490	0.498
σ_0 (N/m)	560.0	549.4	554.1	556.7	550.6
σ_1 (N/(m/s))	300.0	291.0	294.2	303	299.8

Table 2. Standard deviation of friction parameters.

	Least Square Algorithm	Genetic Algorithm	Ant Colony Algorithm	Proposed Algorithm
F_s (N)	0.279	0.229	0.251	0.119
v_s (rad/s)	0.0292	0.0166	0.0112	0.0052
σ_0 (N/m)	26.92	19.98	21.97	14.34
σ_1 (N/(m/s))	23.45	16.19	20.74	11.57

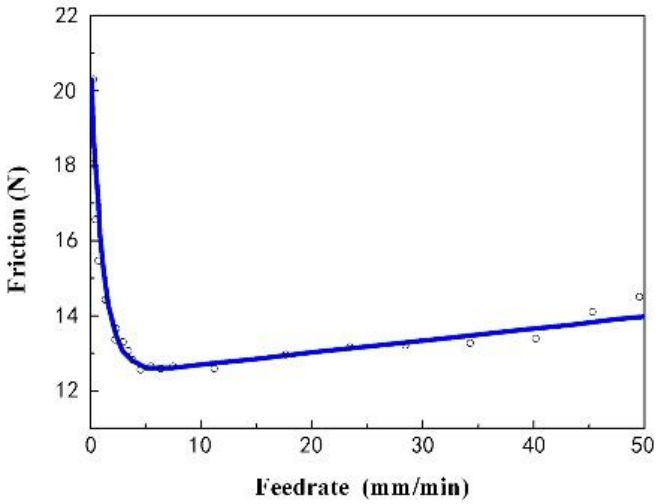


Figure 4. Relationship diagram of friction and velocity.

2.3. Tracking Error Modeling

To improve the overall contour machining accuracy of the PMLSM, it is crucial to address the issue of deviation between the actual position and the theoretical position caused by friction. The complex curvature trajectory often results in sliding and crawling, which exacerbates the problem. Analyzing the tracking error attributable to friction offers an opportunity to enhance the increment accuracy of the PMLSM. Taking the *X*-axis for an example, the system state space expression is shown as follows:

$$\begin{cases} y = x_1 \\ \dot{x}_1 = x_2 \\ \dot{x}_2 = -\alpha_2 x_1 - \alpha_1 x_2 + \beta u_x - \frac{1}{m} F_f + \frac{1}{m} d \end{cases} \tag{15}$$

Substituting (15) into (1), the state equations can be expressed as follows:

$$\begin{cases} y = x_1 \\ \dot{x}_1 = x_2 \\ \dot{x}_2 = -\alpha_2 x_1 - \alpha_1 x_2 + \beta u_x - \frac{1}{m}\left(\sigma_0 \xi - \sigma_1 \frac{d\xi}{dt} + \sigma_2\right) + \frac{1}{m} d \end{cases} \tag{16}$$

where $\alpha_1 = c_1/m, \alpha_2 = K/m, \beta = k_F \cdot k_u/m$.

m—mass matrix;
c_1—equivalent viscosity coefficient;
K—Stiffness coefficient;
k_F—thrust coefficient;
k_u—amplifier gain;
μ_x—input control;
d—disturbance.

Supposing the theoretical position is x_d, the feed error is $\dot{e}_1$, the acceleration deviation is $\dot{e}_2$,

$$\begin{cases} \dot{e}_{f1} = e_{f2} \\ \dot{e}_{f2} = \ddot{x}_d + \alpha_2 x_1 + \alpha_1 x_2 - \beta u_x + \frac{1}{m}\left(\sigma_0 \xi - \sigma_1 \frac{d\xi}{dt} + \sigma_2\right) - \frac{1}{m} d \end{cases} \tag{17}$$

Thus, the tracking error can be obtained by solving the differential equation with the given error state space expression e_f.

3. Friction Compensation and Control Strategy

3.1. Friction Feedforward Control Design

The problem of error compensated signal has been a major obstacle in the traditional method of controlling the motion accuracy of linear motors through feedback [33]. To overcome this difficulty and improve precision machining, a feedforward control compensator strategy has been designed. This strategy estimates and adjusts the tracking error caused by friction before it is input into the motor, thus avoiding cycle delay and improving the motion-tracking accuracy of a single axis. The schematic diagram of X-axis as an example is shown in Figure 5.

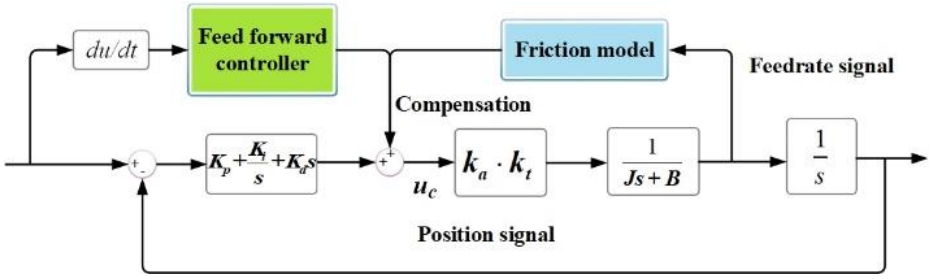


Figure 5. Friction compensation model.

The simulation structure diagram of the LuGre model, shown in Figure 6, utilizes the velocity feedback as input to calculate the parameters. To estimate the friction force, the average elastic deformation is obtained through simulation since the bristle z, being an intermediate state variable, cannot be accurately determined. The position tracking accuracy control performance of the linear motor is improved by superimposing the tracking error compensation, adjusted by feedforward control, with the theoretical data. Furthermore, Figure 6 illustrates the simulation block diagram of the friction feedforward controller.

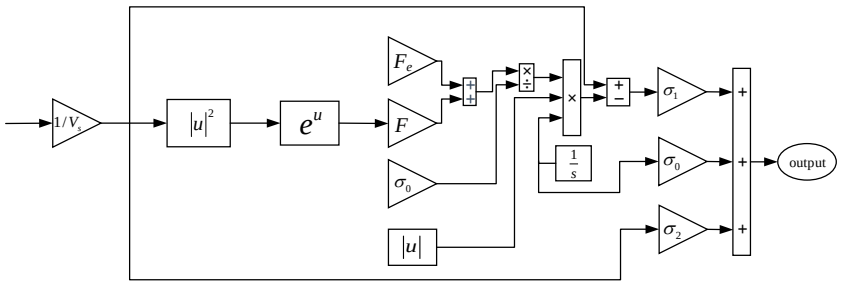


Figure 6. Simulation diagram of LuGre model.

Shown in Figure 7, the comparison of simulated results for friction compensation reveals that the feedforward compensation strategy effectively mitigates friction disturbance during linear motion. The maximum friction is reduced by over 50%, and the fluctuation of friction compensation remains stable. Consequently, it is evident that this control strategy enhances the tracking performance of linear motors and improves the contour accuracy of precision machining.

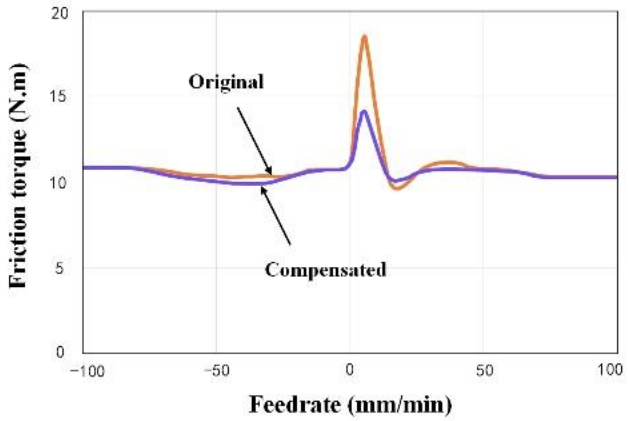


Figure 7. Simulated comparison of friction compensation.

3.2. Experiment of Friction Compensation Control

The effectiveness and necessity of friction feedforward control were verified by comparing experiments. The friction feedforward control was tested using the experiment of complex curves on the precision machining platform, as shown in Figure 8. The experimental path consisted of straight lines and curves, with a total length of 600 mm and a feed rate of 500 mm/min. Since friction hindered the motion of the linear motor, it resulted in a reduction in tracking accuracy. Therefore, the tracking error was considered as the index for friction compensation.

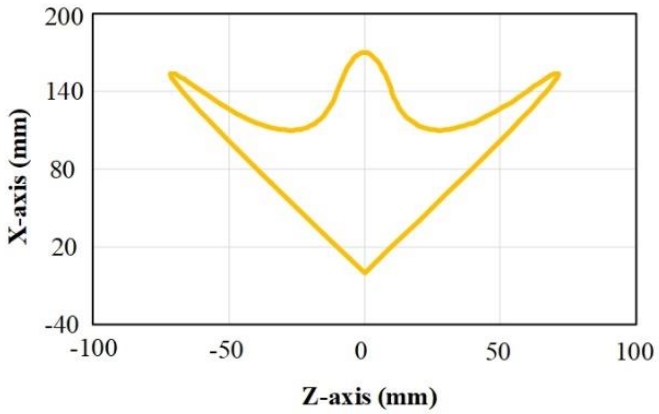


Figure 8. B-spline Complex path.

The comparison results of the tracking error were shown in Figure 9. Figure 9a–f show the *X*-axis tracking errors, respectively, Figure 9g–l show the *Z*-axis tracking errors, respectively. As comparisons, the mirror compensation, sliding model control, adaptive fuzzy control, and adaptive neural network control were introduced. As shown in Figure 9, the maximum tracking errors of the *X*-axis were 3.98 μm, −3.53 μm, 3.76 μm, 3.58 μm, −3.24 μm, and 3.13 μm, respectively, and the standard deviations were 0.892 μm, 0.861 μm, 0.835 μm, 0.823 μm, 0.786 μm, 0.701 μm, respectively. Meanwhile, the maximum tracking errors of the *Z*-axis were −3.71 μm, −3.25 μm, −3.61 μm, −3.65 μm, −2.76 μm, −2.78 μm, respectively, and the standard deviations were 0.658 μm, 0.655 μm, 0.652 μm, 0.634 μm,

0.601 µm, 0.542 µm, respectively. It was obvious that the proposed method can effectively reduce tracking errors caused by friction and improve the motion accuracy of linear motors. Although other methods can also reduce tracking errors, the proposed algorithm had a more significant improvement; the maximum tracking accuracy can be improved by 25.1% at the sharp corner, which outperformed the traditional method in terms of compensation performance.

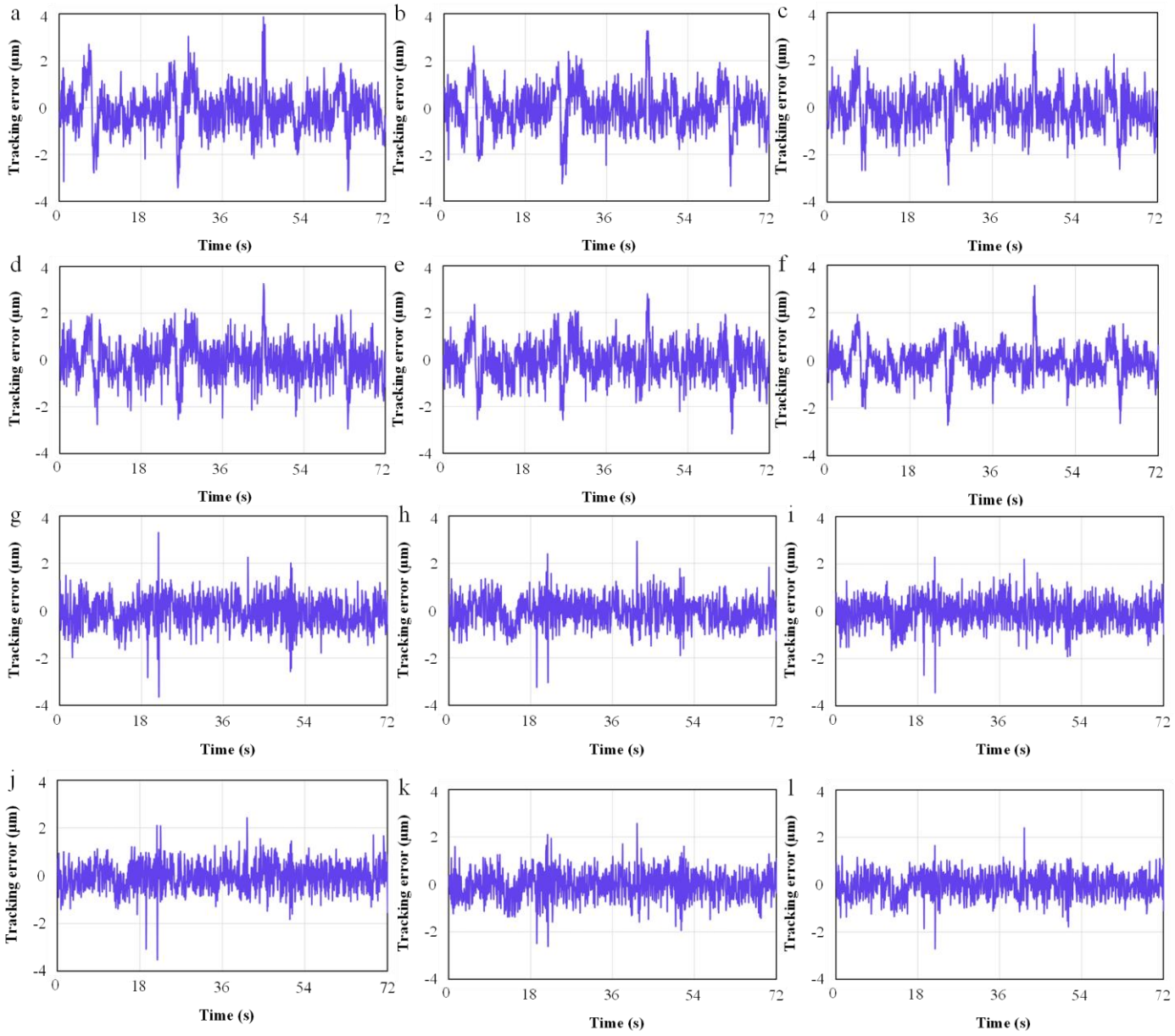


Figure 9. Compensation result of tracking errors. ((**a**–**f**) were the *X*-axis tracking errors, (**g**–**l**) were the *Z*-axis tracking errors. (**a**,**g**) were the original errors, (**b**,**h**) were the mirror compensation, (**c**,**i**) were the sliding model control compensation, (**d**,**j**) were the adaptive fuzzy control compensation, (**e**,**k**) were the adaptive neural network control compensation, (**f**,**l**) were the proposed method).

The research of friction disturbance can enrich the analysis of motion tracking accuracy of linear motor. In addition, friction can also influence the feed rate. This deviation can be reduced by feedforward control compensation. Figure 10 shows the comparison results of feed rate fluctuation error before and after compensation. It can be seen that the maximum error decreased from 2.8 mm/min to 2.3 mm/min, and the average decreased by 0.19 mm/min. After compensation, the machine tool feed is more uniform and more smooth, which suppresses

the error caused by friction to some extent. Furthermore, the friction feedforward compensation strategy enhances the tracking accuracy, thus providing a foundation for improving the overall machining contour accuracy of the precision machining platform.

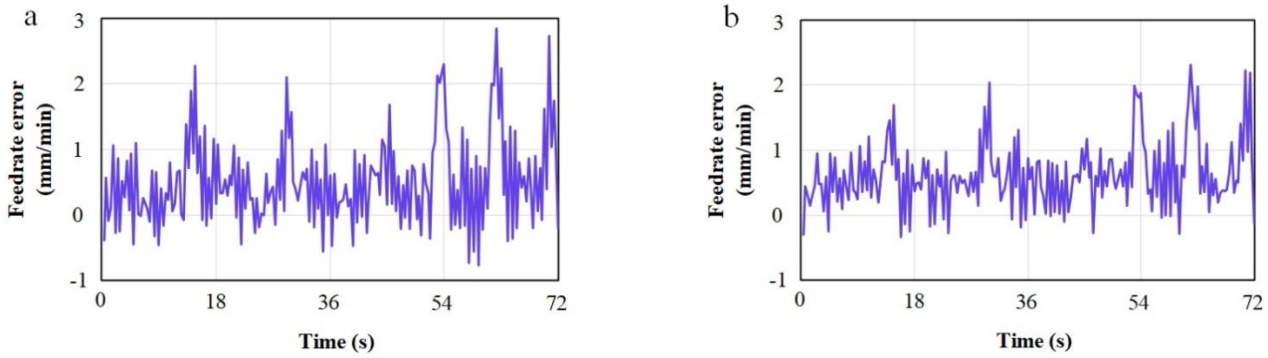


Figure 10. Compensation result of feed rate error. (**a**) Before compensation; (**b**) After compensation.

4. Contour Error Modeling and Controlling

4.1. Contour Error Modeling

In the Figure 11, the contour error can be defined as $\boldsymbol{\varepsilon} = \boldsymbol{P_n} - \boldsymbol{P_a}$ where $\boldsymbol{P_n}$ is the nearest point from the actual point on the designed trajectory to the actual point. To calculate the contour error, the proximate point $\boldsymbol{P_e}$ is used to calculate the contour error. Therefore, $\boldsymbol{\varepsilon}$ is replaced by an estimated contour error $\hat{\boldsymbol{\varepsilon}}$,

$$\hat{\boldsymbol{\varepsilon}} = [\hat{\varepsilon}_x, \hat{\varepsilon}_y, \hat{\varepsilon}_z]^T = \boldsymbol{P_e} - \boldsymbol{P_a} \tag{18}$$

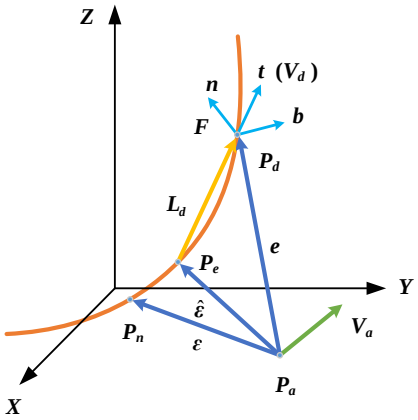


Figure 11. Calculation model of space contour error.

As shown in the Figure 11, the unit orthogonal tangent vector $\boldsymbol{t}$ and normal vector n and bi-normal vector $\boldsymbol{b} = \boldsymbol{t} \times \boldsymbol{n}$ vectors along with reference path are computed by

$$\boldsymbol{t} = \frac{\dot{\boldsymbol{P}}_d}{\left\|\dot{\boldsymbol{P}}_d\right\|}, \quad \boldsymbol{n} = \frac{\ddot{\boldsymbol{P}}_d}{\left\|\ddot{\boldsymbol{P}}_d\right\|} \tag{19}$$

and the Frenet Frame consists of the three vectors, $\boldsymbol{F} = [\boldsymbol{t}(\mathrm{t}), \boldsymbol{n}(t), \boldsymbol{b}(t)]$. Then, the tracking error $\boldsymbol{e}$ is transformed into the Frenet Frame

$$\boldsymbol{e} = \boldsymbol{F}\boldsymbol{e}_{\boldsymbol{F}} \leftrightarrow \ \boldsymbol{e}_{\boldsymbol{F}} = \boldsymbol{F}^{-1}\boldsymbol{e} = [e_t, e_n, e_b]^T \tag{20}$$

Finally, the delay time $\boldsymbol{t_d}$ of contour error is

$$t_d = \frac{e_t}{\left\|\dot{\boldsymbol{P}}_{\boldsymbol{d}}\right\|} \tag{21}$$

In order to calculate the $\boldsymbol{P_e}$ using Taylor expansion, the delay displacement $\boldsymbol{L} = \boldsymbol{V_d} \cdot t_d \approx \boldsymbol{P_d}(t - t_d) - \boldsymbol{P_d}(t) = \boldsymbol{P_e} - \boldsymbol{P_d}$ and estimated contour error $\hat{\boldsymbol{\varepsilon}} = \boldsymbol{e} - \boldsymbol{L}$ are determined. It is worth noting that both $\boldsymbol{P_d}(t)$ and $\boldsymbol{P_d}(t_d)$ lie on the reference path, implying that the modeling accuracy is higher than that of the traditional method, where the estimated point often deviates from the design trajectory.

4.2. Influence of the Dynamic Parameter on Contour Error

In this section, the influence of the inertia of each axis parameter on the contour error will be discussed. As mentioned above, improving the single-axis tracking accuracy alone may not significantly improve the contour accuracy. This is mainly because the contour error is caused by the uncoordinated motion of each axis and the differences in inertia between them, making it difficult to directly compensate for the contour error. In the system, the input and output have the following relationship:

$$T_i \frac{dR_i(t)}{dt} + R_i(t) = K_{ci} D_i(t) \quad i = x, y, z \ldots \tag{22}$$

where T_i is the motion period constant, R_i is the actual trajectory, D_i is the designed trajectory, and K_{ci} is the close loop gain. Taking the shell parts as an example on the precision machining platform, when the radius of circular trajectory is R,

$$x^2 + y^2 = R^2 \quad \Leftrightarrow \quad \begin{cases} x_d(t) = \frac{R}{K_{cx}} \cos \omega t \\ y_d(t) = \frac{R}{K_{cy}} sin\omega t \end{cases} \tag{23}$$

Substituting into (23), the steady-state solution of the system can be expressed as follows:

$$\begin{cases} x_r(t) = \frac{R}{K_{cx}} \frac{1}{\sqrt{1+(T_x\omega)^2}} \cos(\omega t - \arctan T_x\omega) \\ y_r(t) = \frac{R}{K_{cy}} \frac{1}{\sqrt{1+(T_y\omega)^2}} \cos(\omega t - \arctan T_y\omega) \end{cases} \tag{24}$$

For shell parts, the deviation between the actual trajectory and the designed path can be expressed as follows:

$$e_r = \frac{1}{2R}\left[x_r^2(t) + y_r^2(t) - R^2\right] \tag{25}$$

With steady-state expansion and ignoring the higher order polynomials, Equation (24) can be rewritten as follows:

$$\begin{aligned} e_r = \quad & -\tfrac{R}{2}\omega^2 t^2 + \tfrac{R}{4}\left[\left(K_{cx} + K_{cy} - 2\right) + \left(2\theta_n^2 - K_{cx}T_x^2\omega^2 - K_{cy}T_y^2\omega^2\right)\right] \\ & + \tfrac{R}{4}\sqrt{a_n^2 + b_n^2}\sin\left(2\omega t + \arctan\tfrac{b_n}{a_n}\right) \end{aligned} \tag{26}$$

where $a_n = 2\omega\left(K_{cy}T_x - K_{cx}T_y\omega\right)$,

$$b_n = K_{cy}\left(1 - 3T_x^2\omega^2\right) - K_{cx}\left(1 - 3T_y^2\omega^2\right).$$

As we can see in Equation (26), e_r is mainly affected by the inertia parameters of each axis system in the second and third items, the details are shown as follows:

(1) When the motion time and dynamic gains of each axis are equal, the second and third terms of equation (26) become zero. Consequently, the error er is solely influenced by the first servo dynamic characteristics. In this scenario, the error is dependent on both the frequency of the servo bandwidth and the size of the design path.

(2) When the motion time constants T_x and T_y of each axis are different, but the motion gains K_{cx} and K_{cy} are the same, the Equation (26) can be rewritten as follows:

$$e_r = -\frac{R}{8}\omega^2\left[4t^2 + \left(T_x - T_y\right)^2\right] + \frac{R}{2}\omega t\frac{T_x - T_y}{t}\sin 2\omega t \tag{27}$$

(3) Except for the first item, error er is affected by two parts based on (27). One part is constant and independent of time. The other part consists of elliptic trajectories that vary with time. These trajectories have a major axis distributed in the direction of 45° or 135°, and their radius is related to the system dynamic parameter ωt.

(4) When the motion time constants T_x and T_y are equal, but the motion gains K_{cx} and K_{cy} are different, Equation (26) can be rewritten as follows:

$$\begin{aligned} e_r = \quad & -\tfrac{R}{2}\omega^2t^2 - \tfrac{R}{8}\left(\omega^2t^2 - 1\right)\left(\tfrac{K_{cx}-K_{cy}}{t}\right)^2 \\ & +\tfrac{R}{2}\left(1 - \omega^2t^2\right)\tfrac{K_{cx}-K_{cy}}{t}\sin\left(2\omega t + \tfrac{\pi}{2}\right) \end{aligned} \tag{28}$$

In this case, the error e_r can be compared to the second case, where the error curve resembles an ellipse. The major and minor axes of this ellipse are correlated with the radius of the intended path.

(5) When T_x, T_y and K_{cx}, K_{cy} are all different, Equation (27) can be rewritten as follows:

$$\begin{aligned} e_r = \quad & -\tfrac{R}{2}\omega^2t^2 \\ & -\tfrac{R}{8}\omega^2t^2\left[\left(\tfrac{T_x-T_y}{t} + \tfrac{K_{cx}-K_{cy}}{t}\right)^2 - R\left(\tfrac{K_{cx}-K_{cy}}{t}\right)^2\right] \\ & +\tfrac{R}{2}\left\{1 + \tfrac{\omega^2t^2}{2}\left[\left(\tfrac{T_x-T_y}{K_{cx}-K_{cy}} - 1\right)^2 - 3\right]\right\}\tfrac{K_{cx}-K_{cy}}{t}\sin 2\omega t \end{aligned} \tag{29}$$

Equation (29) shows the relationship between the error e_r and the parameters of each axis, and the trend of e_r is similar to the second and third cases.

From the above analysis, it can be observed that the contour error of a linear servo system is influenced by several factors. These include the command signal frequency, the curvature of the designed path, the system frequency response, and the motion dynamic gain of each axis. Merely enhancing the tracking accuracy of a single axis does not effectively reduce the overall contour error. Therefore, it is crucial to consider the problem of inertia matching and error compensation coordination of each axis.

4.3. Design of Cross-Coupled Control Strategy

In this section, a three-axis cross-coupled controller is designed to adjust and control the estimated contour error. The central controller, represented by $\boldsymbol{K_{cc}}$ and consisting of a Fuzzy PID controller, plays a crucial role in the entire CCC system as it determines the accuracy of compensation. $\boldsymbol{K_{ci}}$ and $\boldsymbol{G_i}$ (i = x, y, z) are the position controller and controlled object, respectively. The estimated contour error, as shown in Figure 12, is input into the central controller, which generates an error control signal by coupling it with the parameters of each axis. The compensation of the contour error is then decoupled to each axis in proportion and superimposed with the theoretical point $\boldsymbol{R_d} = \left[R_{dx}, R_{dy}, R_{dz}\right]$. This process enables the prediction and compensation of the contour error. The actual position $\boldsymbol{R_a} = \left[R_{ax}, R_{ay}, R_{az}\right]$, meanwhile, serves as a reference for comparison. To facilitate the controller design and ensure consistency, the motion cycle parameters of each axis are set to the same value, $T_x = T_y = T_z$.

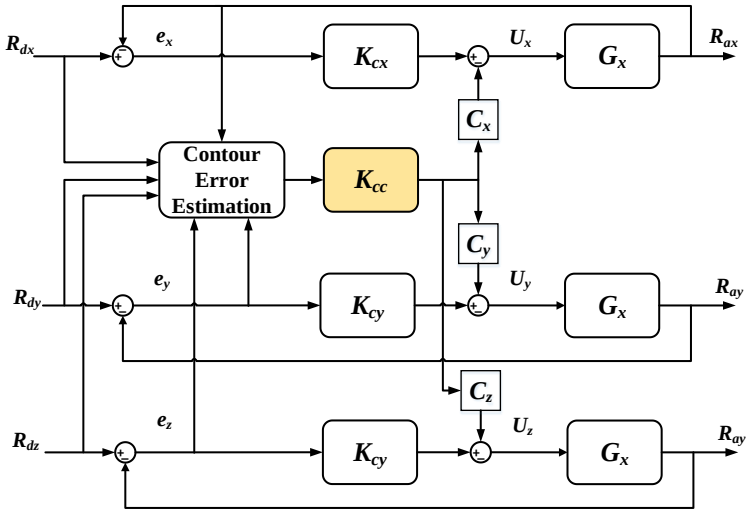


Figure 12. Central controller of cross-coupled controller.

Firstly, it is assumed that the contour error is $\Delta\varepsilon$ when a cross-coupled controller is not added, that is to say $K_{cc} = 0$, as known in Figure 12, where K_{ci} and G_i (i = x, y, z) are the position controller and the controlled object. When the CCC is adopted, the contour error can be expressed as follows:

$$\Delta\varepsilon = \frac{1}{1 + K_{cx}G_x} C_x R_{dx} + \frac{1}{1 + K_{cy}G_y} C_y R_{dy} + \frac{1}{1 + K_{cz}G_z} C_z R_{dz} \tag{30}$$

$$\varepsilon = \frac{\Delta\varepsilon}{1 + \left(\frac{1}{1+K_{cx}G_x} C_x^2 G_x + \frac{1}{1+K_{cy}G_x} C_y^2 G_y + \frac{1}{1+K_{cz}G_z} C_z^2 G_z\right) K_{cc}} \tag{31}$$

In actual machining, the main factor that affects contour accuracy is the mismatch of parameters in multi-axis. This mismatch leads to an uneven distribution of contour error throughout the whole trajectory. To address this issue, a pre-compensation strategy is proposed. The strategy takes advantage of the curvature variation characteristics of the spline path to reduce the contour error. Additionally, it considers the inertia matching and coordination of the parameters in each axis to improve the machining contour accuracy. A complex B-spline path of simulation, with a total length of 742 mm and a feed rate of 1400 mm/min, was shown in Figure 13. As shown in Figure 14, the maximum tracking errors of the x-axis and y-axis were reduced by 47.01% and 47.02%, respectively, while the contour error was reduced by 46.5%. Consequently, the proposed strategy significantly improved the contour error.

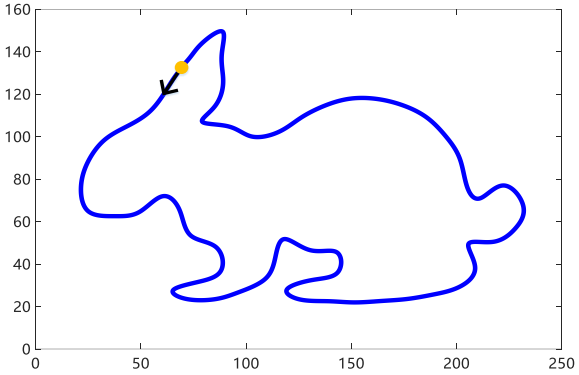


Figure 13. B-spline complex spline path.

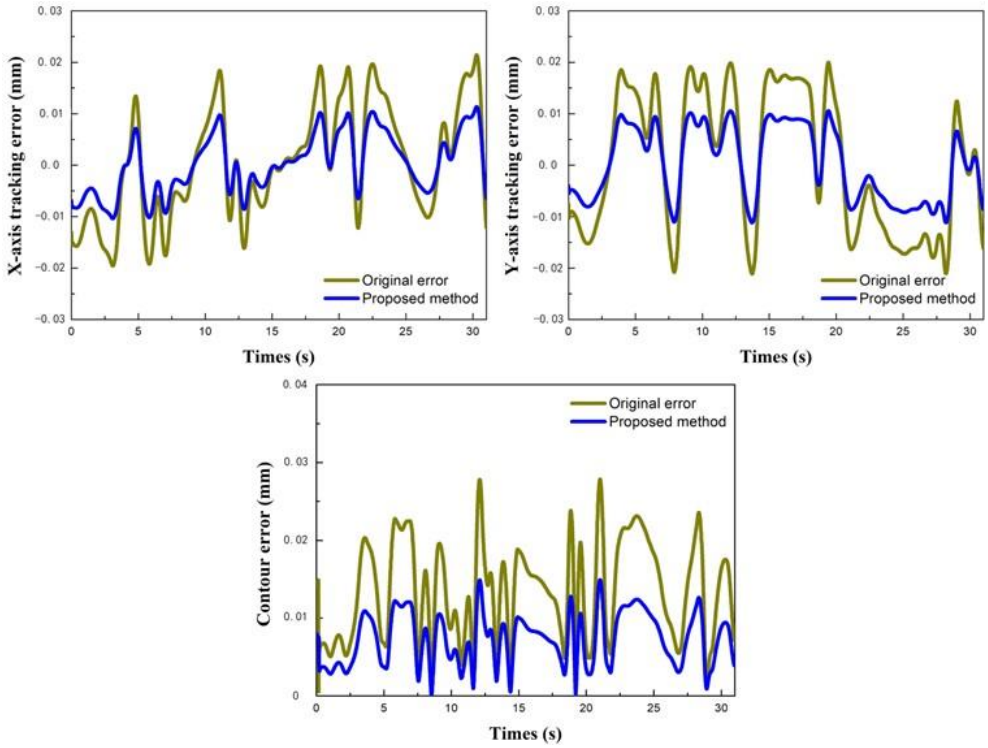


Figure 14. Error contrastive results of pre-compensation of CCC.

5. Machining Experiment Verification

The effectiveness of the proposed friction control strategy on the precision turning and grinding integrated machining platform, shown in Figure 15, was verified by the precision machining of shell parts. The shell was made of aluminum (7075) and had a radius of 120 mm and a wall thickness of 3 mm. The machining parameters were as follows: a speed of 450 r/min, a feed rate of 10 mm/min, and a cutting depth of 0.005 mm. The shell parts were cut using a carbide turning tool, and the cutting mode from the bottom to the top of the shell was selected to ensure machining quality and cutting integrity. In this experiment, the effect of the cutting force was ignored due to the small cutting depth. During the machining process, friction hindered the feed movement of the machine tool, resulting in a reduction in tracking accuracy and the overall contour accuracy of the parts. Therefore, in this section, the compensation effect of each axis tracking error was used as the standard to measure the performance of the proposed friction control strategy and to verify its effectiveness and necessity.

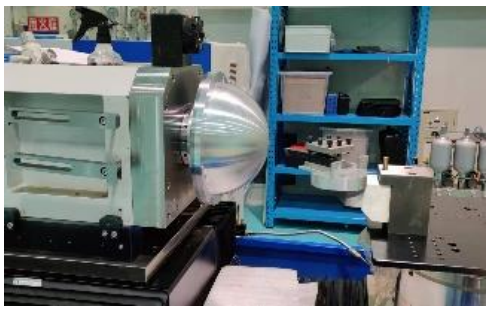


Figure 15. Machining experiment of spherical shell.

Due to dynamic friction disturbance, the accuracy of the linear motor decreases with high feed rate. In Figure 16, the original tracking errors of the *X*-axis and *Z*-axis were represented by a and c, respectively. Friction compensation control for the *X*-axis and *Z*-axis was denoted by b and d, respectively. The control compensation strategy based on the LuGre friction model can significantly reduce the tracking error and contour error. The

thrust fluctuation caused the error to fluctuate periodically, resulting in slightly different compensation effects at different positions. As shown in Figures 16 and 17, the tracking error was reduced from 1.41 μm and 0.81 μm to 1.02 μm and 0.50 μm, respectively. In addition, the contour accuracy was improved from 1.81 μm to 1.43 μm. The friction control compensation strategy further refined the motion analysis of the linear motor, improved tracking accuracy, and laid the foundation for enhancing the overall contour accuracy of the precision machining platform.

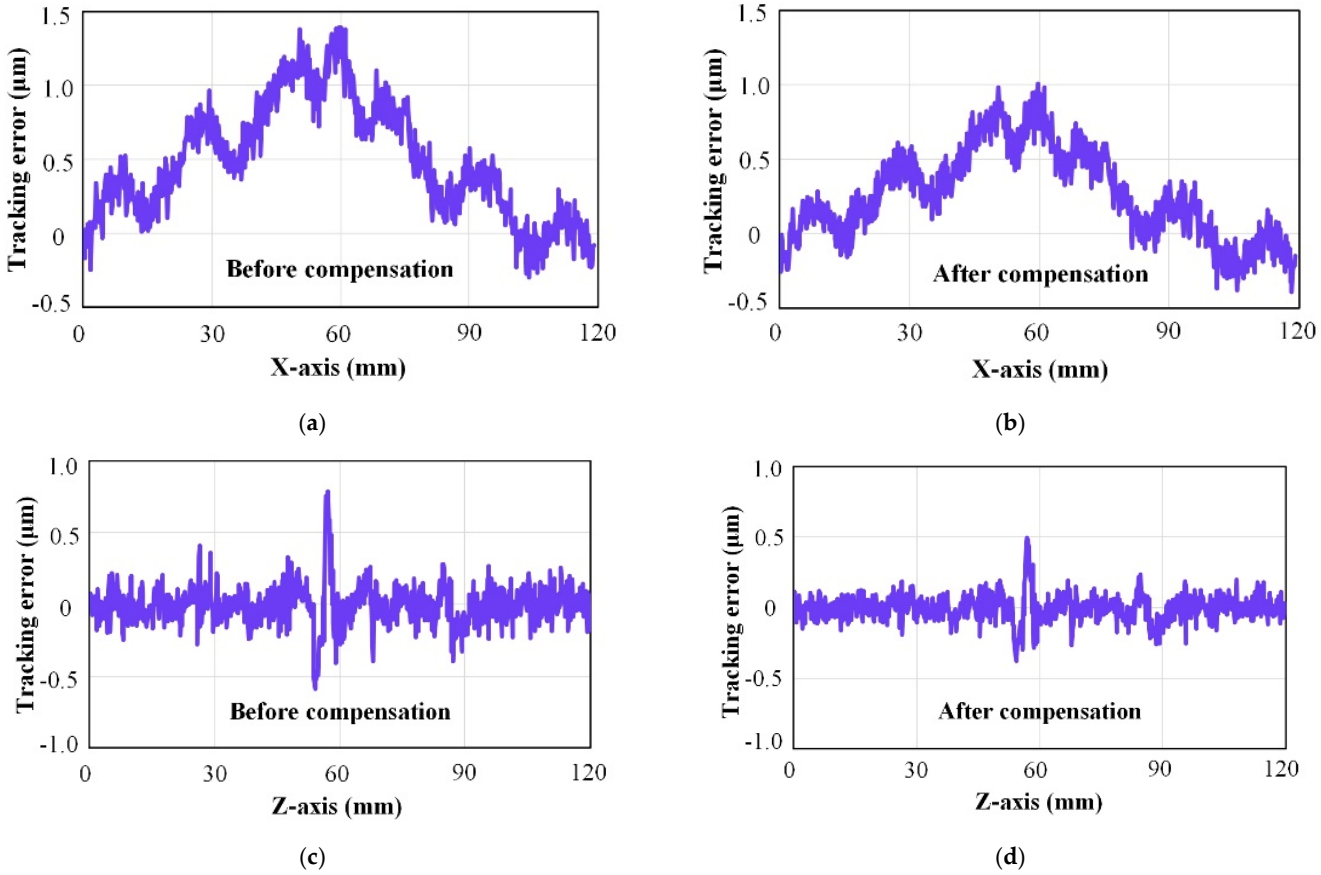


Figure 16. Compensation result of tracking error. ((**a**,**b**) were the before and after compensation of X-axis, (**c**,**d**) were the before and after compensation of Z-axis).

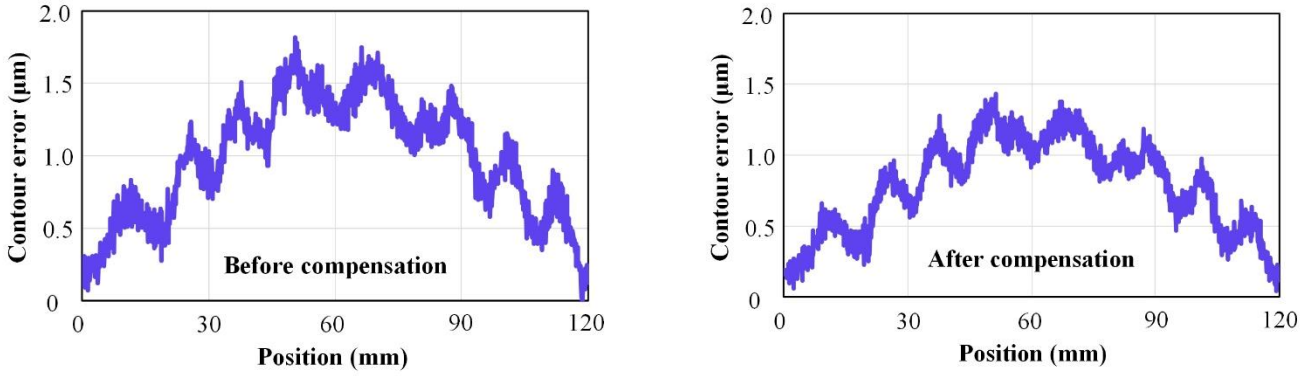


Figure 17. Compensation result of contour error.

6. Conclusions

To improve machining accuracy in precision machining, several strategies are employed. Firstly, the LuGre model is utilized for dynamic friction modeling, with the

dynamic and static parameters accurately identified using the improved Drosophila multi-objective parameters optimization algorithm. Through state space analysis, the expression of tracking error caused by friction is derived. Additionally, a feedforward compensation strategy is implemented to address the periodic signal delay issue present in traditional friction control models. Secondly, a pre-compensated cross-coupled control strategy is designed to regulate and distribute compensative values to each axis. This strategy takes into account the mismatch problem arising from the inertia parameters of each axis, ensuring accurate control over the contour error. The experimental results indicate that this friction compensation strategy can reduce the tracking error by up to 25.1%, thereby guaranteeing precise motion control of the machine tool under extreme conditions.

Author Contributions: M.L.: revision, formal analysis, validation. Y.Z.: revision, formal analysis. H.X.: revision. W.L.: writing—original draft, project administration, supervision, funding acquisition. H.Y.: investigation and funding acquisition. X.G.: investigation. All authors have read and agreed to the published version of the manuscript.

Funding: This work was funded by the Basic Scientific Research Projects of Liaoning Provincial Department of Education (Grant No. JYTMS20231454), National Science Foundation support projects, China (Grant No. 62003014), and the College Students Innovative Entrepreneurial Training Plan Program (Grant No. S202410148042).

Data Availability Statement: All the data presented in this study are contained in the article's main text.

Conflicts of Interest: The authors declare no conflicts of interest.

References

1. Jiang, S.L.; Sun, Y.W. Stability analysis for a milling system considering multi-point-contact cross-axis mode coupling and cutter run-out effects. *Mech. Syst. Signal Process.* **2020**, *141*, 106452. [CrossRef]
2. Sun, Y.W.; Jia, J.; Xu, J.T.; Chen, M.; Niu, J. Path, feedrate and trajectory planning for free-form surface machining: A state-of-the-art review. *Chin. J. Aeronaut.* **2022**, *35*, 12–29. [CrossRef]
3. Yan, S.C.; Sui, L.; Wang, S.Q.; Sun, Y.W. On-line tool wear monitoring under variable milling conditions based on a condition-adaptive hidden semi-Markov model (CAHSMM). *Mech. Syst. Signal Process.* **2023**, *200*, 110644. [CrossRef]
4. Liu, W.; Bai, X.; Yang, H.; Bao, R.; Liu, J. Tendon driven bistable origami flexible gripper for high-speed adaptive grasping. *IEEE Robot. Autom. Lett.* **2024**, *9*, 5417–5424. [CrossRef]
5. Guo, Q.; Liu, Z.L.; Yang, Z.; Jiang, Y. Development, challenges and future trends on the fabrication of micro-textured surfaces using milling technology. *J. Manuf. Process.* **2024**, *126*, 285–331. [CrossRef]
6. Armstrong-Hélouvry, B.; Dupont, P.; Wit, C.C.D. A survey of models, analysis tools and compensation methods for the control of machines with friction. *Automatica* **1994**, *30*, 1083–1138. [CrossRef]
7. Simba, K.R.; Bui, B.D.; Msukwa, M.R.; Uchiyama, N. Robust iterative learning contouring controller with disturbance observer for machine tool feed drives. *ISA Trans.* **2018**, *75*, 207–215. [CrossRef]
8. Li, C.B.; Pavelescu, D. The friction-speed relation and its influence on the critical velocity of stick-slip motion. *Wear* **1982**, *82*, 277–289.
9. Dahl, P.R. Solid friction damping of mechanical vibrations. *AIAA J.* **1976**, *14*, 1675–1682. [CrossRef]
10. de Wit, C.C.; Olsson, H.; Astrom, K.; Lischinsky, P. A new model for control of systems with friction. *IEEE Trans. Autom. Control* **1995**, *40*, 419–425. [CrossRef]
11. Freidovich, L.; Robertsson, A.; Shiriaev, A.; Johansson, R. Friction compensation based on LuGre model. In Proceedings of the IEEE Conference on Decision & Control, San Diego, CA, USA, 13–15 December 2006.
12. Bicakci, S.; Akdas, D.; Karaoglan, A.D. Optimizing Karnopp friction model parameters of a pendulum using RSM. *Eur. J. Control* **2014**, *20*, 180–187. [CrossRef]
13. Swevers, J.; Al-Bender, F.; Ganseman, C.; Projogo, T. An integrated friction model structure with improved presliding behavior for accurate friction compensation. *IEEE Trans. Autom. Control* **2000**, *45*, 675–686. [CrossRef]
14. Chu, H.; Gao, B.; Gu, W.; Chen, H. Low-speed control for permanent-magnet DC torque motor using observer-based nonlinear triple-step controller. *IEEE Trans. Ind. Electron.* **2017**, *64*, 3286–3296. [CrossRef]
15. Cui, P.; Zhang, D.; Yang, S.; Li, H. Friction compensation based on time-delay control and internal model control for a gimbal System in magnetically suspended CMG. *IEEE Trans. Ind. Electron.* **2017**, *64*, 3798–3807. [CrossRef]
16. Liu, D.; Tao, T.; Mei, C.S. Study on the decoupling identification method of linear dynamic and nonlinear friction for servo driver system. *Chin. J. Sci. Instrum.* **2010**, *31*, 782–788.
17. Ba, D.B.; Simba, K.R.; Uchiyama, N. Contouring control for three-axis machine tools based on nonlinear friction compensation for lead screws. *Int. J. Mach. Tools Manuf.* **2016**, *108*, 95–105.

18. Kim, S.J.; Ha, I.J. A frequency-domain approach to identification of mechanical systems with friction. *IEEE Trans. Autom. Control* **2001**, *46*, 888–893.
19. Du, F.; Li, P.; Wang, Z.; Yue, M.; Feng, X. Modeling, identification and analysis of a novel two-axis differential micro-feed system. *Precis. Eng.* **2017**, *50*, 320–327. [CrossRef]
20. Sanxiu, W.; Yunbo, Z.; Guang, C. LuGre friction compensation control of servo manipulator based on neural network. *J. Beijing Univ. Technol.* **2016**, *42*, 679–683.
21. Zhu, H.; Fujimoto, H. Mechanical deformation analysis and high-precision control for ball-screw-driven stages. *IEEE Trans. Mechatron.* **2015**, *20*, 956–966. [CrossRef]
22. Lin, C.J.; Yau, H.T.; Tian, Y.C. Identification and compensation of nonlinear friction characteristics and precision control for a linear motor stage. *IEEE Trans. Mechatron.* **2012**, *18*, 1385–1396. [CrossRef]
23. Iwasaki, M.; Shibata, T.; Matsui, N. Disturbance-observer-based nonlinear friction compensation in table drive system. *IEEE/ASME Trans. Mechatron.* **1999**, *4*, 3–8. [CrossRef]
24. Rafan, N.; Jamaludin, Z.; Chiew, T.; Abdullah, L.; Maslan, M. Contour error Analysis of precise positioning for ball screw driven stage using friction model feedforward. *Procedia CIRP* **2015**, *26*, 712–717. [CrossRef]
25. Koren, Y. Cross-coupled biaxial computer control for manufacturing systems. *J. Dyn. Syst. Meas. Control.* **1980**, *102*, 265–272. [CrossRef]
26. Koren, Y.; Lo, C.C. Variable-gain cross-coupling controller for contouring. *CIRP Ann.-Manuf. Technol.* **1991**, *40*, 371–374. [CrossRef]
27. Su, K.H.; Cheng, M.Y. Contouring accuracy improvement using cross-coupled control and position error compensator. *Int. J. Mach. Tools Manuf.* **2008**, *48*, 1444–1453. [CrossRef]
28. Huo, F.; Poo, A.N. Improving contouring accuracy by using generalized cross-coupled control. *Int. J. Mach. Tools Manuf.* **2012**, *63*, 49–57. [CrossRef]
29. Marques, F.; Woliński, Ł.; Wojtyra, M.; Flores, P.; Lankarani, H.M. An investigation of a novel LuGre-based friction force model. *Mech. Mach. Theory* **2021**, *166*, 104493. [CrossRef]
30. Liang, K.; Tu, Q.Z.; Shen, X.M.; Fang, Z.H.; Yang, X.; Zhang, Y.; Xiang, H.Y. An improved LuGre model for calculating static steering torque of rubber tracked chassis. *Def. Technol.* **2022**, *18*, 797–810. [CrossRef]
31. Ghodsi, M.; Mohammadzaheri, M.; Soltani, P.; Ziaifar, H. A new active anti-vibration system using a magnetostrictive bimetal actuator. *J. Magn. Magn. Mater.* **2022**, *557*, 169463. [CrossRef]
32. Yu, Y.; Li, Y.; Li, J. Parameter identification and sensitivity analysis of an improved LuGre friction model for magnetorheological elastomer base isolator. *Soft Mechatron.* **2015**, *50*, 2691–2707. [CrossRef]
33. Wan, M.; Dai, J.; Zhang, W.-H.; Xiao, Q.-B.; Qin, X.-B. Adaptive feed-forward friction compensation through developing an asymmetrical dynamic friction model. *Mech. Mach. Theory* **2022**, *170*, 104691. [CrossRef]

Disclaimer/Publisher's Note: The statements, opinions and data contained in all publications are solely those of the individual author(s) and contributor(s) and not of MDPI and/or the editor(s). MDPI and/or the editor(s) disclaim responsibility for any injury to people or property resulting from any ideas, methods, instructions or products referred to in the content.